LETTER

Antibacterial membrane attack by a pore-forming intestinal C-type lectin

Sohini Mukherjee[1], Hui Zheng[2], Mehabaw G. Derebe[1], Keith M. Callenberg[3], Carrie L. Partch[4], Darcy Rollins[1], Daniel C. Propheter[1], Josep Rizo[5], Michael Grabe[3]†, Qiu-Xing Jiang[2]* & Lora V. Hooper[1,6]*

Human body-surface epithelia coexist in close association with complex bacterial communities and are protected by a variety of antibacterial proteins. C-type lectins of the RegIII family are bactericidal proteins that limit direct contact between bacteria and the intestinal epithelium and thus promote tolerance to the intestinal microbiota[1,2]. RegIII lectins recognize their bacterial targets by binding peptidoglycan carbohydrate[1,3], but the mechanism by which they kill bacteria is unknown. Here we elucidate the mechanistic basis for RegIII bactericidal activity. We show that human RegIIIα (also known as HIP/PAP) binds membrane phospholipids and kills bacteria by forming a hexameric membrane-permeabilizing oligomeric pore. We derive a three-dimensional model of the RegIIIα pore by docking the RegIIIα crystal structure into a cryo-electron microscopic map of the pore complex, and show that the model accords with experimentally determined properties of the pore. Lipopolysaccharide inhibits RegIIIα pore-forming activity, explaining why RegIIIα is bactericidal for Gram-positive but not Gram-negative bacteria. Our findings identify C-type lectins as mediators of membrane attack in the mucosal immune system, and provide detailed insight into an antibacterial mechanism that promotes mutualism with the resident microbiota.

RegIIIα damages the surfaces of Gram-positive bacteria[1], indicating that RegIIIα might target bacterial membranes. We assessed the capacity of RegIIIα to permeabilize bacterial membranes by quantifying bacterial uptake of a membrane-impermeant fluorescent dye (SYTOX green). RegIIIα increased SYTOX green uptake when added to the Gram-positive species *Listeria monocytogenes*, indicating damaged membranes (Fig. 1a, b). RegIIIα has an anionic amino-terminal pro-segment that inhibits bactericidal activity (but not peptidoglycan binding) by docking to the protein core through charge–charge interactions[4]. The pro-segment is removed by trypsin on secretion into the intestinal lumen, yielding bactericidally active RegIIIα (ref. 4). Bactericidally inactive pro-RegIIIα did not induce SYTOX green uptake, indicating minimal membrane permeabilization (Fig. 1a). Thus, RegIIIα permeabilizes the bacterial membrane, and the pro-segment inhibits this activity.

To test directly for membrane disruption by RegIIIα we used liposomes composed of 85% zwitterionic phospholipid (PC) and 15% acidic phospholipid (PS). The liposomes encapsulated carboxyfluorescein, a fluorescent dye. RegIIIα induced rapid dye efflux from PC/PS liposomes (Fig. 1c), which was reduced when PC-only liposomes were used (Fig. 1d, e). This indicates a preference for acidic phospholipids that is consistent with the acidic lipid content of bacterial membranes[5] and with the salt sensitivity of RegIIIα membrane toxicity (Extended Data Fig. 2a, b). These findings indicate that RegIIIα interactions with lipid bilayers are mediated by electrostatic interactions. pro-RegIIIα yielded a diminished rate of dye release (Fig. 1f), indicating that the pro-segment inhibits membrane permeabilization.

We next assessed RegIIIα lipid-binding activity by measuring changes in the intrinsic fluorescence of tryptophan residues[6]. We observed increased tryptophan fluorescence intensity only when RegIIIα was added to PS-containing liposomes (Fig. 1g–i), indicating that RegIIIα interacts with acidic phospholipids. Furthermore, we observed fluorescence resonance energy transfer (FRET) between donor RegIIIα tryptophan residues and dansyl-labelled PC/PS liposomes[7] (Fig. 1j, k). FRET was inhibited by the pro-RegIIIα N-terminal pro-segment (Fig. 1j, k), indicating that the pro-segment inhibits bactericidal activity by hindering lipid binding. Consistent with its inability to bind lipids, pro-RegIIIα did not inhibit RegIIIα bactericidal activity in mixing experiments (Extended Data Fig. 2c).

Several membrane-active toxins destabilize membranes by forming monomeric or multimeric pores[8]. To test for RegIIIα pores, we performed conductance studies in black lipid membranes, a model system that mimics the properties of a cell membrane[9]. RegIIIα produced rapid single-channel-like currents at −80 mV in the presence of Mg^{2+} ions (Fig. 2a), with no current detected at 0 mV. Using the Nernst–Planck equation we estimated the diameter of the pore at ~12–14 Å (Extended Data Fig. 3). The calculated pore size agreed with the lack of efflux of fluorescein isothiocyanate-dextran-10 (FD10) or FD4, which have Stokes diameters of ~44 Å and ~28 Å, respectively (Fig. 2b). In contrast, carboxyfluorescein (~10 Å) passed readily through the pores (Figs 1c and 2b). These results show that RegIIIα forms functional transmembrane pores and yield an estimate of the inner pore diameter.

When visualized by negative-stain electron microscopy (EM), numerous circular structures of ~100 Å diameter were observed on liposomes incubated with RegIIIα (Fig. 2c and Extended Data Fig. 4a). Although RegIIIα is a monomer in solution[10], the size of the pores suggested that they were RegIIIα multimers. We therefore treated liposome-associated RegIIIα with a crosslinking agent, solubilized the products in detergent, and separated them by size-exclusion chromatography (Fig. 2d). In addition to a prominent monomer peak we detected a second, liposome-dependent peak at a lower retention volume, indicating the formation of a multimeric complex. Western blotting showed a single RegIIIα species with mobility similar to that predicted for a hexamer (Fig. 2d), suggesting that the pore was a RegIIIα hexamer.

After longer incubations with lipid, RegIIIα formed filaments (Extended Data Fig. 4b) similar to those in pancreatic secretions[11]. The filaments were ~100 Å in diameter, correlating with the dimensions of the RegIIIα pore (Fig. 2c). RegIIIα filamentation required lipid and was dependent on RegIIIα pore formation, as pro-RegIIIα formed neither pores nor filaments (Extended Data Fig. 4b, d). Filamentation partially inhibited the ability of RegIIIα to permeabilize membranes (Extended Data Figs 4c and 5a–c), as observed with other membrane toxic host defence proteins where filamentation traps pore complexes and limits damage to host cells[12]. These findings indicate that the RegIIIα filaments
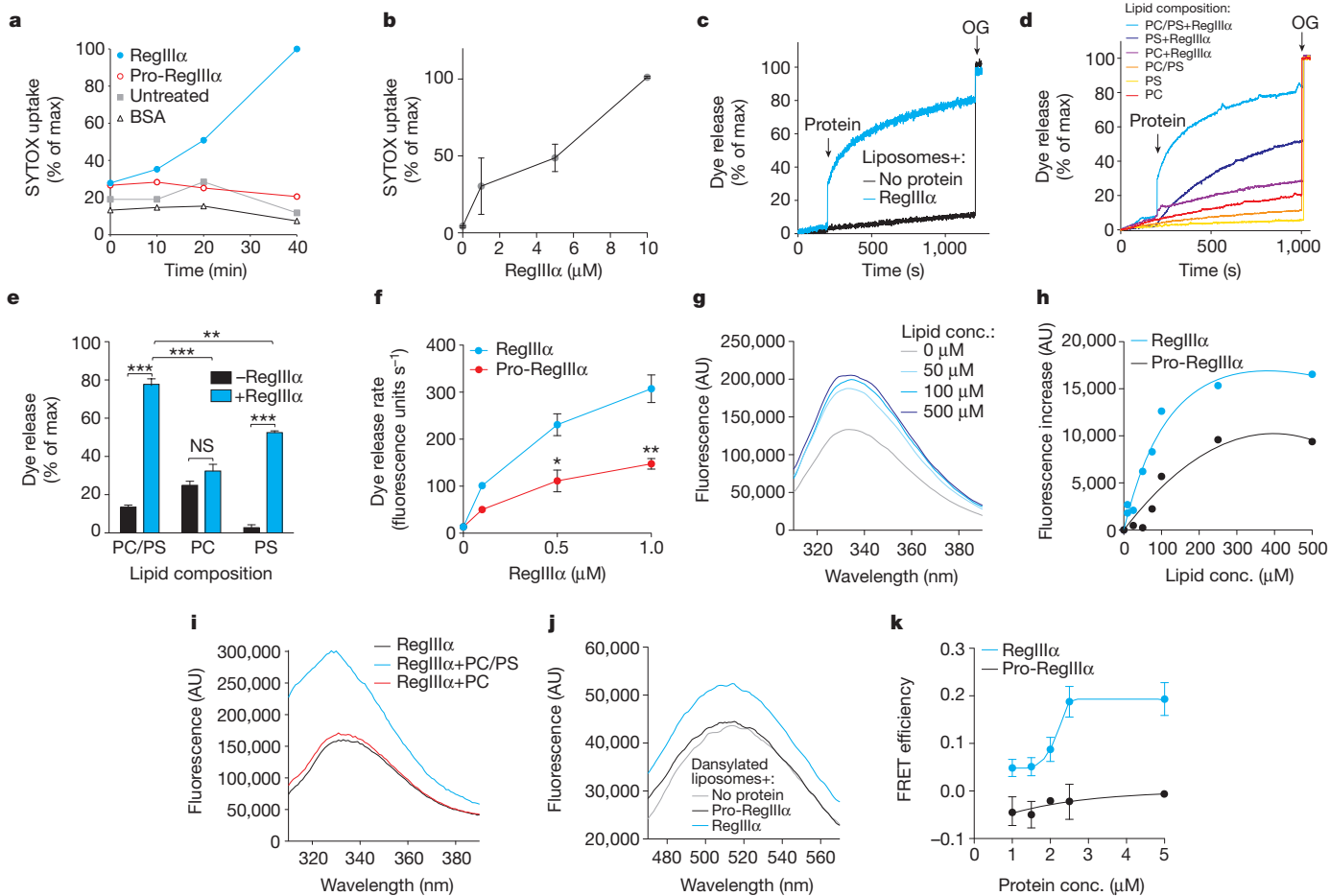
Figure 1 | RegIIIα permeabilizes the bacterial membrane. a, *Listeria monocytogenes* was treated with 25 μM RegIIIα, pro-RegIIIα, or BSA or left untreated, and bacterial uptake of SYTOX green was measured. Results are representative of three independent experiments, and are expressed as a percentage of maximum SYTOX uptake in the presence of 0.2% SDS. **b**, SYTOX green uptake by *L. monocytogenes* in the presence of increasing RegIIIα concentrations. Assays were performed in triplicate. Means ± s.e.m. are plotted. **c**, Carboxyfluorescein (CF)-loaded liposomes (10 μM lipid; 85% PC/15% PS) were treated with 1 μM RegIIIα. 1.0% octylglucoside (OG) was added towards the end to disrupt remaining liposomes. Dye efflux is expressed as percentage of maximal release by detergent. Results are representative of five independent experiments. **d**, 10 μM RegIIIα was added to carboxyfluorescein-loaded liposomes (100 μM lipid; 100% PC, 100% PS or 85% PC:15% PS), and dye efflux was monitored over time. Representative results are shown.

e, Averaged results from three independent replicates of the experiment shown in **d**. NS, not significant; $**P < 0.01$; $***P < 0.001$. **f**, Initial rate of liposome dye efflux (100 μM lipid) as a function of RegIIIα and pro-RegIIIα concentration. Results are representative of three independent experiments. $*P < 0.05$; $**P < 0.01$. **g**, Intrinsic tryptophan fluorescence of 1 μM RegIIIα was measured in the presence of increasing lipid concentrations. **h**, Tryptophan fluorescence of 1 μM RegIIIα and pro-RegIIIα as a function of lipid concentration. **i**, Intrinsic tryptophan fluorescence of 1 μM RegIIIα was measured in the presence of liposomes (100 μM lipid) of varying lipid composition. **j**, 5.0 μM RegIIIα or pro-RegIIIα was added to liposomes (100 μM lipid) incorporating 5% dansyl-PE and dansyl fluorescence was monitored. Assays were performed in triplicate. **k**, FRET efficiency as a function of RegIIIα and pro-RegIIIα concentration. Assays were performed in triplicate. Means ± s.e.m. are plotted.

are higher-order assemblies of RegIIIα pore complexes and show that filamentation limits RegIIIα toxicity.

Although the ~90-kDa RegIIIα pore complex was too small for structure determination by single-particle cryoelectron microscopy (cryoEM) methods[13], the RegIIIα filaments were sufficiently large for such analysis. We therefore reconstructed a three-dimensional map of the RegIIIα filament and extracted the structure of the minimal pore complex (Fig. 3a, b and Extended Data Fig. 6a–f). The nominal resolution of our structure, 9.2 Å, was limited by symmetry variability and filament bending (Extended Data Fig. 6g–j and Supplementary Information). Consistent with our crosslinking studies (Fig. 2d), the minimal pore was a hexamer formed by three RegIIIα dimers related by helical symmetry. The outer diameter of the pore assembly was 89 Å, as observed by negative-stain EM (Fig. 2c). The pore height was 55 Å, sufficient to span a lipid bilayer (35–45 Å)[14]. The inner diameter was ~18 Å, consistent with the pore size predicted by our conductance measurements (Extended Data Fig. 3) and dye release assays (Fig. 2b).

RegIIIα, like other epithelial bactericidal proteins such as α-defensins, is constrained by disulphide bonds that prohibit large secondary structure changes on moving from an aqueous to an apolar environment[15,16]. This suggested the feasibility of docking the three-dimensional structure of the RegIIIα monomer into the EM density map to model the organization of the pore complex further. First, we determined the crystal structure of processed, bactericidally active RegIIIα (Extended Data Fig. 7a) and compared it to the previously determined structure of bactericidally inactive pro-RegIIIα. The two structures were similar, although the amino acid side chains of the loop encompassing residues 93–99 (sequence KSIGNSY) adopted different orientations in the active RegIIIα structure (Fig. 3c). This was consistent with the conformational flexibility of this loop as indicated by a higher crystallographic B-factor (Extended Data Fig. 7b).

The active RegIIIα structure could be docked into the cryo-EM hexameric density map (Fig. 3d and Extended Data Fig. 6k, l), providing good spatial constraints for building a hexameric model. The model indicates that the RegIIIα subunits in the pore assembly are
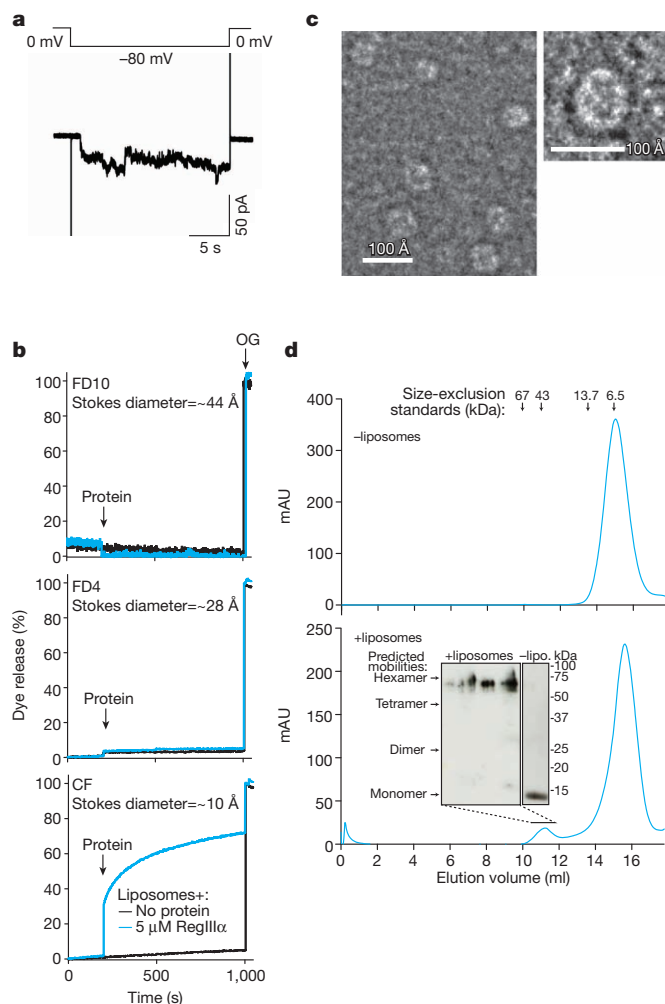
Figure 2 | RegIIIα forms a transmembrane pore. a, RegIIIα-dependent current flow across a planar lipid bilayer is depicted as a function of time. No current was observed before the application of a voltage across the membrane. Upon the application of −80 mV, inward current was observed, and returning the membrane potential to zero diminished the current because the measured reverse potential was −4.0 mV. The current trace is representative of multiple independent experiments. **b**, Liposomes loaded with FITC-Dextran 10 (FD10), FITC-Dextran 4 (FD4), or carboxyfluorescein (CF) were treated with 5.0 μM RegIIIα and dye release was monitored over time. 1% OG (octylglucoside) was added to disrupt the liposomes towards the end of the experiment. **c**, Negative-stain electron microscopy (EM) images of RegIIIα in the presence of lipid bilayers. An individual RegIIIα pore particle is shown in the right-hand panel. **d**, RegIIIα (100 μM) in the presence or absence of liposomes (1 mM lipid) was crosslinked with 5 mM 1-ethyl-3-[3-dimethylaminopropyl]carbodiimide hydrochloride (EDC). Crosslinked complexes were solubilized in detergent, resolved by size-exclusion chromatography, and analysed by western blotting with anti-RegIII antibody. The predicted mobilities of RegIIIα dimers, tetramers and hexamers were calculated from the mobility of the monomer after crosslinking in the absence of liposomes (right panel in blot).

oriented with the carbohydrate-binding loop pointing towards the central channel, and the loop encompassing residues 93–99 and the N and carboxy (C) termini oriented towards the lipid bilayer (Fig. 3d). The resolution of our map did not allow us to extract detailed information about intermolecular interactions in the pore complex. There was imperfect docking of the carbohydrate-binding loop, the loop encompassing residues 93–99, and the far N terminus (Fig. 3d), consistent with the conformational flexibility of these regions (Extended Data Fig. 7b).

We used mutagenesis to assess experimentally the orientation of RegIIIα in the pore complex. Our model predicts that the basic residue

Lys 93 is oriented towards the lipid bilayer (Fig. 3d) and thus might be involved in interactions with the negatively charged phospholipids required for RegIIIα–liposome interactions (Fig. 1d, e). A Lys93Ala mutation, but not conservative Lys93Arg and Lys93His mutations, reduced the toxicity of RegIIIα for liposomes as well as intact bacteria (Fig. 3e, f and Extended Data Fig. 8a). In contrast, a Glu114Gln mutation, which resides in the carbohydrate-binding loop (Fig. 3c)[3], did not have an impact on membrane toxicity, consistent with its predicted position near the pore interior (Fig. 3d, e). As expected, the Lys93Ala mutation but not the Glu114Gln mutation inhibited filament formation (Extended Data Fig. 8b). Finally, the orientation of the N terminus towards the lipid bilayer is consistent with the role of the N-terminal pro-segment in inhibiting RegIIIα interactions with lipid and reducing membrane toxicity (Fig. 1a, f, h, j, k).

We next calculated the energetics of pore insertion into a PC-like membrane bilayer using physics-based computational modelling (Extended Data Fig. 9a–d)[17]. The model predicts that basic residues are located near the membrane–water interface whereas a strip of hydrophobic and polar residues is buried in the membrane core (Fig. 3g). The complex presents a positive electric field to the membrane (Extended Data Fig. 9e, f), creating an unfavourable electrostatic energy unless negatively charged PS-like lipids are added to the membrane (Fig. 3h). This is consistent with our finding that PS lipids are necessary for RegIIIα toxicity (Fig. 1d, e). Finally, calculations on the Lys93Ala mutant showed reduced stability (Fig. 3h) due to loss of favourable electrostatic interactions between Lys 93 and negatively charged lipids. Thus, the model reveals that charge sequestration is a critical determinant of RegIIIα pore stability in the membrane. Furthermore, the model predicts that Arg 166 interacts with the membrane surface (Extended Data Fig. 10a). Consistent with this prediction, an Arg166Ala mutation reduced membrane toxicity of RegIIIα (Extended Data Fig. 10b). In contrast, mutating Arg 39, which is exposed to aqueous solvent in the model, had little effect on RegIIIα membrane toxicity (Extended Data Fig. 10a, b). Thus, our model accurately predicts the experimental behaviour of the RegIIIα pore.

RegIIIα selectively targets Gram-positive bacteria[1], raising the question of why RegIIIα cannot kill Gram-negative bacteria by permeabilizing the outer membrane. In contrast to PC/PS liposomes, liposomes composed of an *Escherichia coli* total lipid extract were not disrupted by RegIIIα (Fig. 4a), indicating that a component of the lipid extract inhibited membrane permeabilization. Lipopolysaccharide (LPS), a major constituent of the Gram-negative outer membrane, inhibited RegIIIα-mediated liposome disruption and antibacterial activity (Fig. 4b, c), indicating that LPS is one factor that prevents RegIIIα-mediated permeabilization of Gram-negative bacteria.

Finally, we postulated that the trypsin-cleavable inhibitory N terminus of pro-RegIIIα evolved to suppress pore-forming activity and thus minimize cytotoxicity during RegIIIα synthesis and storage in epithelial cells. In support of this idea, RegIIIα was cytotoxic towards cultured intestinal epithelial cells (MODE-K)[18], and the pro-segment suppressed this cytotoxicity (Fig. 4d, e).

Thus, RegIIIα kills its bacterial targets by oligomerizing on the bacterial membrane to form a membrane-penetrating pore (Extended Data Fig. 1). Membrane attack by pore formation represents a previously unappreciated biological activity for the C-type lectin family. Our findings may provide insight into the evolutionary origins of the lectin-mediated complement pathway, in which recruited complement proteins disrupt microbial membranes[19]. With its intrinsic capacity for membrane attack, RegIIIα may represent a more evolutionarily primitive mechanism of lectin-mediated innate immunity. We propose that the lectin-mediated complement pathway could have evolved from a directly bactericidal ancestral lectin, with the bacterial recognition function retained by the descendent C-type lectin(s) and the membrane attack function assumed by recruited accessory proteins that assemble into the membrane attack complex.
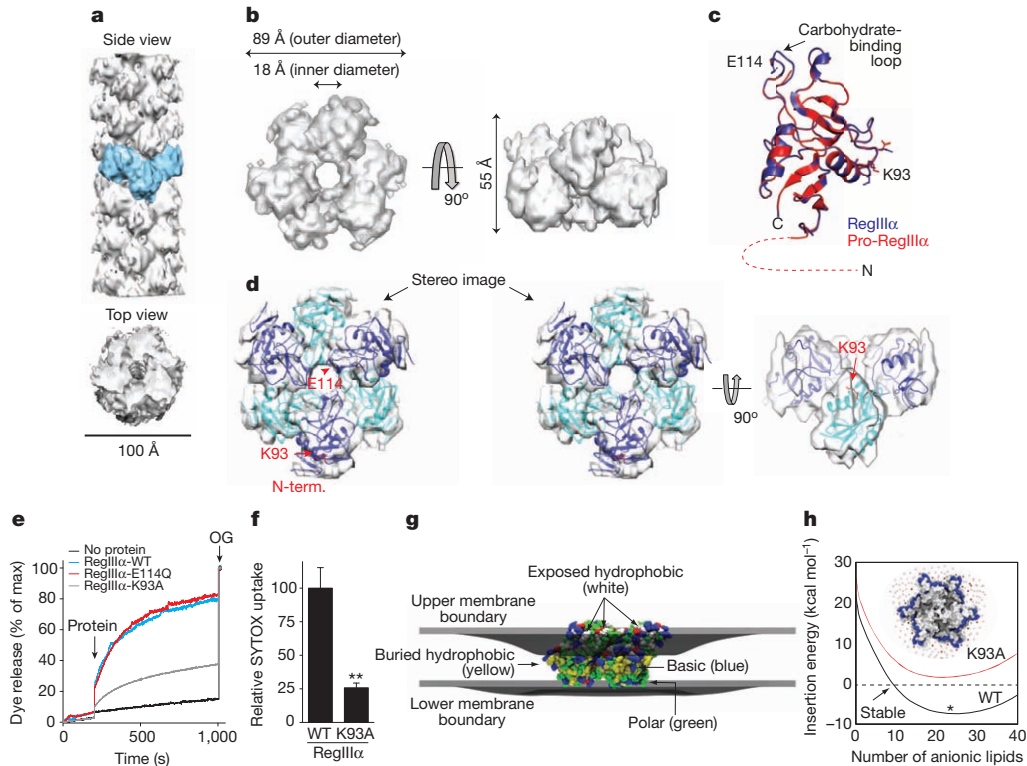
Figure 3 | Structural model of the RegIIIα pore complex. a, Top and side view of the cryoEM reconstruction of the RegIIIα filament. **b**, Top and side view of the cryoEM map of the RegIIIα hexameric complex at a nominal 9.2 Å resolution. **c**, Ribbon representation of the crystal structure of active monomeric RegIIIα (Protein Data Bank (PDB) code 4MTH), aligned with the pro-RegIIIα structure (PDB code 1UV0). The first ten residues of the N-terminal pro-segment are disordered and are therefore missing from the structure; these residues have been depicted as a dashed red line. Side chains in the loop encompassing amino acids 93–99 (KSIGNSY) are shown as sticks. **d**, Stereo diagram showing docking of the active RegIIIα crystal structure into the cryoEM density map. The docked structures are alternately coloured blue and cyan to aid in visualization of the individual subunits. The positions of Lys 93 (K93) and Glu 114 (E114) are indicated. **e**, 5 μM of wild-type (WT), Lys93Ala (K93A) mutant, or Glu114Gln (E114Q) mutant RegIIIα was added to 100 μM carboxyfluorescein-loaded liposomes and dye efflux was monitored. **f**, 1 μM wild-type or Lys93Ala mutant RegIIIα was assayed for membrane disruption in bacteria using the SYTOX uptake assay described in Fig. 1. Assays were performed in triplicate and results are expressed relative to wild-type

RegIIIα. Error bars indicate s.e.m.; **$P < 0.01$. **g**, Most energetically stable membrane configuration around the embedded hexamer. The upper membrane boundary (grey surface) bends down to expose large charged portions of the protein to water, whereas the lower membrane boundary (grey surface) exhibits minor deflections. The region between the upper and lower boundaries is a water-inaccessible region composed of the high-dielectric head-groups and the low-dielectric core. A stretch of hydrophobic residues (yellow) is in the centre of the membrane, whereas charged (basic in blue and acidic in red) and polar (green) residues are near the upper and lower membrane boundaries in the high-dielectric head-group region. **h**, Using the configuration in **g**, we added negatively charged point charges to the head-group regions to model addition of PS lipids (red dots in the inset model). At low values, the total insertion energy for the wild-type protein is positive, indicating a lack of stability, but above 10 negatively charged lipids, the hexamer is stabilized in the membrane (black curve). The optimal lipid configuration is indicated by an asterisk. The insertion energy for the Lys93Ala mutant is in red. Inset: top-down view; red dots, PS lipids; blue, Arg and Lys residues; white dots, uncharged lipid positions.
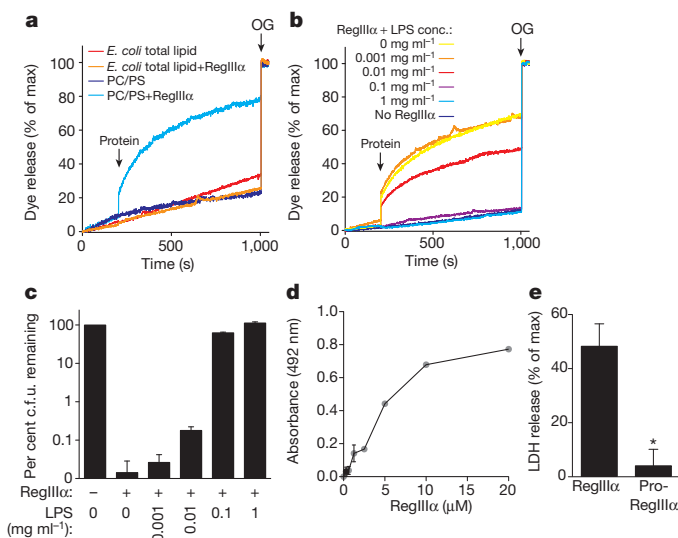

Figure 4 | Regulation of RegIIIα pore formation. a–c, RegIIIα pore formation is inhibited by lipopolysaccharide. **a**, 10 μM RegIIIα was added to liposomes composed of lipids from an *E. coli* total lipid extract or from PC/PS as a control. **b**, 10 μM RegIIIα was added to liposomes (100 μM lipid) in the presence of varying LPS concentrations. **c**, 10 μM RegIIIα was added to ~10^4 c.f.u. of log phase *L. monocytogenes* in the presence of varying LPS concentrations. The assay was carried out at 37 °C for 2 h, and surviving bacteria were quantified by dilution plating. Assays were done in triplicate. Results in **a–c** are representative of two independent experiments. **d, e**, The RegIIIα N-terminal pro-segment limits toxicity towards mammalian cells. **d**, RegIIIα was added to MODE-K cells and cytotoxicity was determined by quantifying lactate dehydrogenase (LDH) release. LDH activity was assessed by spectrophotometric detection of an enzymatic product of LDH at 492 nm. **e**, 10 μM RegIIIα or pro-RegIIIα was added to MODE-K cells and LDH release was quantified. Maximum LDH release was determined by treating cells with NP-40 detergent.

METHODS SUMMARY

Preparation of recombinant RegIIIα. Recombinant human pro-RegIIIα and RegIIIα were expressed and purified according to published methods[1,4].

Membrane permeabilization assays. *Listeria monocytogenes* was exposed to 25 μM RegIIIα, pro-RegIIIα or bovine serum albumin (BSA), incubated with SYTOX green, and cell-associated fluorescence was quantified. For dye leakage assays, fluorescence of carboxyfluorescein-loaded liposomes was monitored over time on a PTI spectrofluorometer, in the presence or absence of RegIIIα or pro-RegIIIα.

Lipid binding assays. Binding of RegIIIα and pro-RegIIIα to liposomes was measured by monitoring fluorescence resonance energy transfer (FRET) between protein tryptophan residues and dansyl-PE. Fluorescence spectra were recorded on a PTI Spectrofluorometer. Measurements of intrinsic tryptophan fluorescence of RegIIIα in the absence or presence of liposomes were recorded on a PTI Spectrofluorometer between 290 and 450 nm at a fixed excitation wavelength of 280 nm.

Crosslinking experiments. RegIIIα was incubated with liposomes for 20 min followed by 1 h treatment with 5 mM of the crosslinking reagent, EDC, at room temperature. The samples were solubilized with 40 mM *n*-decyl-β-D-maltopyranoside (DM) detergent, separated by size-exclusion chromatography, and analysed by western blotting with detection by anti-RegIIIγ antibody[10].

Determination of the RegIIIα crystal structure. Recombinant RegIIIα lacking the N-terminal pro-segment was crystallized using the sitting-drop vapour diffusion method. We collected X-ray diffraction data at the Advanced Photon Source, Argonne National Laboratory. The structure was determined by molecular replacement using a starting model of the full-length RegIIIα structure, followed by cycles of model building. Further details are available in Supplementary Information.

CryoEM imaging. Images were acquired in a JEOL JEM2200FS FEG transmission electron microscope equipped with an in-column energy filter. Full details are available in Supplementary Information.

Computational modelling studies. Full details are available in Supplementary Information.

Statistical analysis. All *P* values were calculated using the unpaired, two-tailed *t*-test.

Online Content Any additional Methods, Extended Data display items and Source Data are available in the online version of the paper; references unique to these sections appear only in the online paper.

1. Cash, H. L., Whitham, C. V., Behrendt, C. L. & Hooper, L. V. Symbiotic bacteria direct expression of an intestinal bactericidal lectin. *Science* **313**, 1126–1130 (2006).
2. Vaishnava, S. *et al.* The antibacterial lectin RegIIIγ promotes the spatial segregation of microbiota and host in the intestine. *Science* **334**, 255–258 (2011).
3. Lehotzky, R. E. *et al.* Molecular basis for peptidoglycan recognition by a bactericidal lectin. *Proc. Natl Acad. Sci. USA* **107**, 7722–7727 (2010).
4. Mukherjee, S. *et al.* Regulation of C-type lectin antimicrobial activity by a flexible N-terminal prosegment. *J. Biol. Chem.* **284**, 4881–4888 (2009).
5. Zasloff, M. Antimicrobial peptides of multicellular organisms. *Nature* **415**, 389–395 (2002).
6. Kraft, C. A., Garrido, J. L., Leiva-Vega, L. & Romero, G. Quantitative analysis of protein-lipid interactions using tryptophan fluorescence. *Sci. Signal.* **2**, l4 (2009).
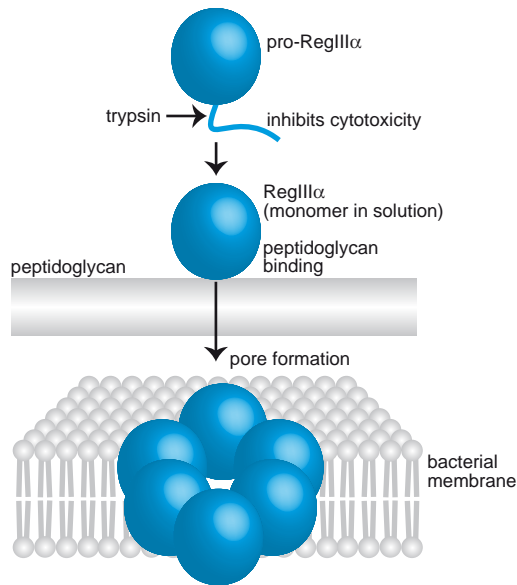7. Fernandez, I. *et al.* Three-dimensional structure of the synaptotagmin 1 C2B-domain: synaptotagmin 1 as a phospholipid binding machine. *Neuron* **32**, 1057–1069 (2001).
8. Brogden, K. A. Antimicrobial peptides: pore formers or metabolic inhibitors in bacteria? *Nature Rev. Microbiol.* **3**, 238–250 (2005).
9. Mueller, P., Rudin, D. O., Tien, H. T. & Wescott, W. C. Reconstitution of cell membrane structure *in vitro* and its transformation into an excitable system. *Nature* **194**, 979–980 (1962).
10. Cash, H. L., Whitham, C. V. & Hooper, L. V. Refolding, purification, and characterization of human and murine RegIII proteins expressed in *Escherichia coli*. *Protein Expr. Purif.* **48**, 151–159 (2006).
11. Ho, M.-R. *et al.* Human pancreatitis-associated protein forms fibrillar aggregates with a native-like conformation. *J. Biol. Chem.* **281**, 33566–33576 (2006).
12. Kagan, B. L. *et al.* Antimicrobial properties of amyloid peptides. *Mol. Pharm.* **9**, 708–717 (2012).
13. Jiang, Q.-X., Wang, D.-N. & MacKinnon, R. Electron microscopic analysis of KvAP voltage-dependent K⁺ channels in an open conformation. *Nature* **430**, 806–810 (2004).
14. Lodish, H. *et al.* in *Molecular Cell Biology* (W.H. Freeman, 2000).
15. Kagan, B. L., Selsted, M. E., Ganz, T. & Lehrer, R. I. Antimicrobial defensin peptides form voltage-dependent ion-permeable channels in planar lipid bilayer membranes. *Proc. Natl Acad. Sci. USA* **87**, 210–214 (1990).
16. Zhang, Y., Lu, W. & Hong, M. The membrane-bound structure and topology of a human α-defensin indicate a dimer pore mechanism for membrane disruption. *Biochemistry* **49**, 9770–9782 (2010).
17. Callenberg, K. M., Latorraca, N. R. & Grabe, M. Membrane bending is critical for the stability of voltage sensor segments in the membrane. *J. Gen. Physiol.* **140**, 55–68 (2012).
18. Vidal, K., Grosjean, I., Revillard, J.-P., Gespach, C. & Kaiserlian, D. Immortalization of mouse intestinal epithelial cells by the SV40-large T gene. Phenotypic and immune characterization of the MODE-K cell line. *J. Immunol. Methods* **166**, 63–73 (1993).
19. Ip, W. K. E., Takahashi, K., Ezekowitz, R. A. & Stuart, L. M. Mannose-binding lectin and innate immunity. *Immunol. Rev.* **230**, 9–21 (2009).

Extended Data Figure 1 | Model of RegIIIα bactericidal function. An overall model that incorporates both the peptidoglycan and lipid-binding functions of RegIIIα is depicted. Combining our current and previous findings, we propose that RegIIIα recognizes and kills its bacterial targets in two distinct steps. First, RegIIIα is secreted from epithelial cells as a soluble monomer that recognizes Gram-positive bacteria by binding to peptidoglycan carbohydrate via an EPN motif located in the long loop region[1,3]. Second, RegIIIα kills bacteria by oligomerizing in the bacterial membrane to form a hexameric membrane-penetrating pore that is predicted to induce uncontrolled ion efflux with subsequent osmotic lysis. The inhibitory N terminus of pro-RegIIIα hinders lipid binding and consequently suppresses pore formation until it is removed by trypsin after secretion into the intestinal lumen[4]. We propose that the inhibitory N-terminal peptide evolved to minimize collateral damage from the RegIIIα pore-forming activity during RegIIIα storage in the membrane-bound secretory granules of epithelial cells. In support of this idea, RegIIIα damages mammalian cell membranes and the N-terminal pro-segment limits this toxicity (Fig. 4d, e).
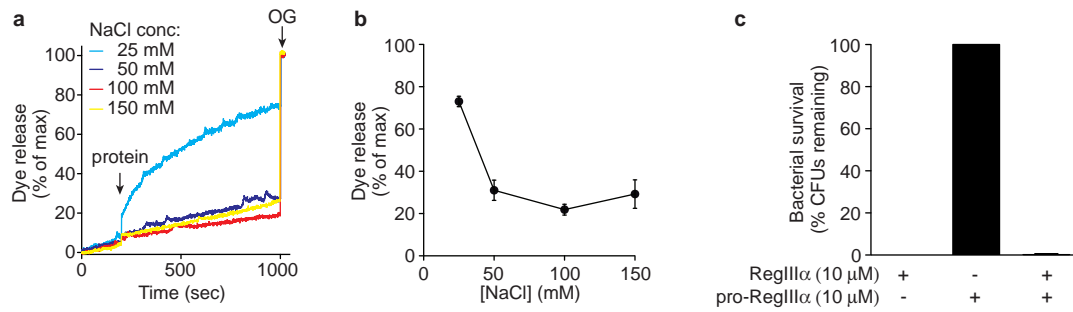
Extended Data Figure 2 | Characterization of RegIIIα membrane permeabilization activity. **a**, **b**, Impact of NaCl concentration on RegIIIα membrane permeabilization activity. **a**, 10 µM RegIIIα was added to liposomes (100 µM lipid) in the presence of varying NaCl concentrations. Representative results are shown. **b**, Averaged results from three independent replicates of the experiment shown in **a**. **c**, Pro-RegIIIα does not inhibit RegIIIα bactericidal activity. 10 µM of purified recombinant pro-RegIIIα, RegIIIα, or a combination of the two was added to $\sim 10^5$ c.f.u. of *L. monocytogenes* for 2 h at 37 °C. Surviving bacteria were quantified by dilution plating.
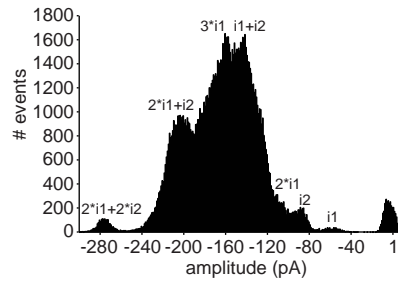
Extended Data Figure 3 | RegIIIα forms a transmembrane pore. Analysis of RegIIIα conductance in lipid bilayers. The trace of a typical single channel recording gave rise to the event histogram shown here. At $-80\,$mV, there was a short latency before the first opening event, which led to the baseline current of $-6.5\,$pA at $-80\,$mV. The baseline current was subtracted so that the baseline corresponds to a peak at 0 pA. Once we assigned two basic peaks at $-53\,$pA and $-81\,$pA as two independent opening events ($i1$ and $i2$), all the other major peaks in the histogram are linear combinations of these two basic events (as labelled). The data therefore suggested two different scenarios. One is that there are three pores, and each pore has two different conducting states, which may reflect the flexible diameter of the pore. The other is that $i1$ and $i2$ reflect two different pores that have different diameters, and that there are at least five different channels in the membrane to produce the observed histogram. This second scenario correlates with the observed variability in helical symmetry. With the idea of variability and protein dynamics in mind, it is likely that the two types of pores may interconvert with each other in the membrane. From the basic events, we estimated the pore diameters by applying the Nernst–Planck equation. In the experimental conditions, our recording chambers had 150 mM K^+, 25 mM Na^+, 215 mM Cl^-, 20 mM Mg^{2+} and 10 mM MES pH 5.5 in the *cis* side, and 20 mM K^+, 25 mM Na^+, 45 mM Cl^- and 10 mM MES pH 5.5 in the *trans* side. The reversal potential (E_K, E_{Na}, E_{Cl} and E_{MES}) for each ion could be calculated ($E_K = 50.9\,$mV, $E_{Na} = 0\,$mV $= E_{MES}$, and $E_{Cl} = -39.5\,$mV). In the *trans* side, there is a trace amount of Mg^{2+} ($\sim$10 μM), which gives a reversal potential E_{Mg} of 92 mV. Our dye leakage assay showed that the pore was open at $V_{mem} = 0\,$mV transmembrane potential, ruling out significant voltage-dependent gating of the RegIIIα channel. On the basis of the ion replacement studies we did for different ions, we estimated the relative permeability of different ions to be: $P_K = P_{Na} = 1.0$; $P_{Cl} = 0.85$; $P_{MES} = 0.73$ and $P_{Mg} = 0.66$. The measured relative permeation rates showed that the pore has very weak cation selectivity, and favours K^+/Na^+ over Mg^{2+} due to the charge density difference. Under the same assumption, the average conductance ($<g>$) of the two basic opening events ($i1$ and $i2$) could be calculated as the following:

$$<g> = \frac{i}{\Sigma P_{ion}(V_{mem} - E_{ion})}$$

The two calculated conductance levels of 100 pS and 152 pS were then entered into the Nernst–Planck equation for electrodiffusion and gave rise to an approximate estimate of the pore diameter of 12 Å and 14 Å, respectively, which is in good agreement with the observed pore size in the reconstructed three-dimensional structure of the pore (Fig. 3b). A more rigorous calculation of the ion flux is possible with a high-resolution picture of the potential profile, but is beyond the scope of this paper.
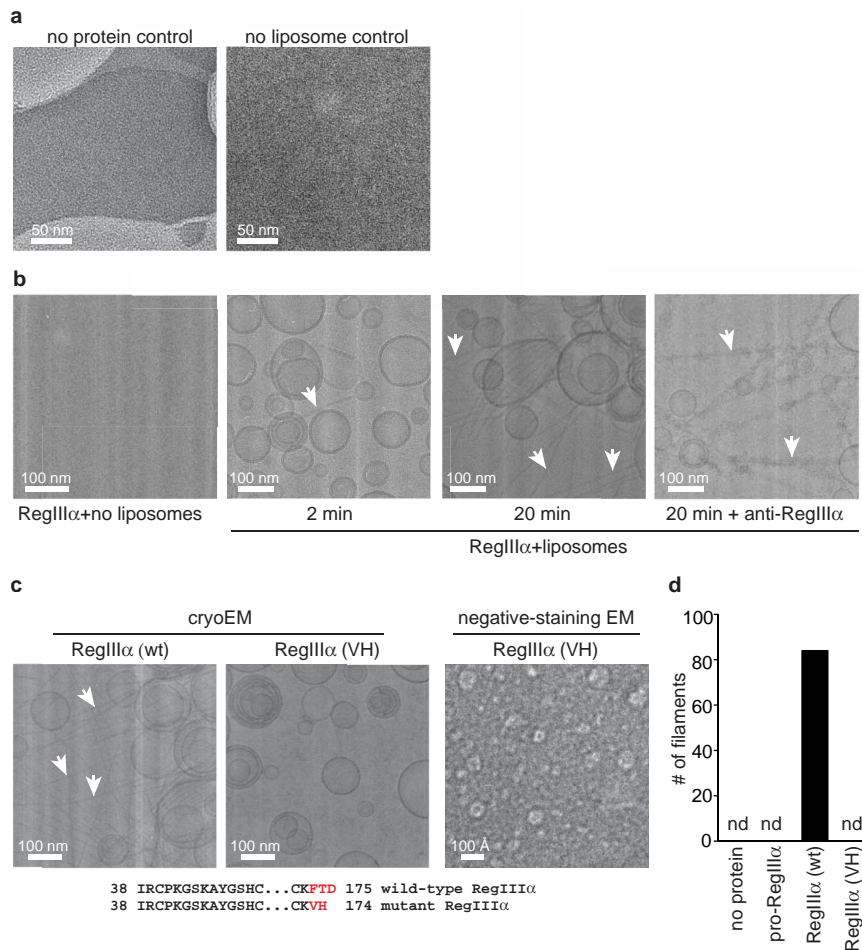
Extended Data Figure 4 | Analysis of liposome-associated RegIIIα by electron microscopy. a, Negative staining EM controls lacking RegIIIα or liposomes are shown. **b–d**, RegIIIα pore complexes assemble into filaments. **b**, RegIIIα forms filaments in the presence of lipid vesicles. 20 μM RegIIIα was incubated for 2 or 20 min with vesicles composed of PC/PS (85%:15%). Samples were visualized by transmission electron microscopy. Grids were stained with anti-RegIII antibody[1,10] to confirm that the filaments were composed of RegIIIα. Filamentation required membranes, as no filaments were observed in the absence of liposomes. Arrows indicate examples of filaments in each image. **c**, 20 μM RegIIIα carrying a mutation near the C terminus (C-terminal sequence: FTD (wild-type)→VH (mutant)) was incubated for 20 min with unilamellar vesicles and visualized by cryoEM and negative-staining EM. The results demonstrate that the VH mutant retains the ability to form pores in lipid bilayers but cannot form filaments. A comparison of the wild-type and mutated C terminus is shown below. **d**, Quantification of filament formation by 20 μM pro-RegIIIα, wild-type (wt) and C-terminal mutant (VH) RegIIIα in the presence of vesicles. Results are representative of counts from three different areas. nd, not detected. The results show that pro-RegIIIα, which cannot form pores, also cannot assemble into filaments.
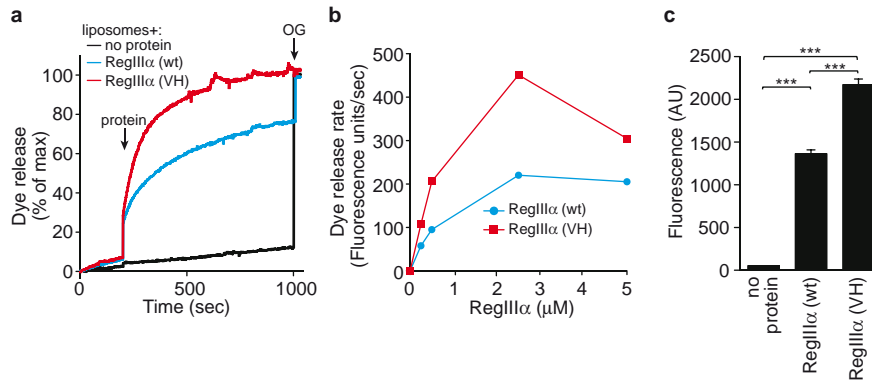
Extended Data Figure 5 | Filament formation inhibits RegIIIα membrane toxicity. We examined the functional properties of the RegIIIα VH mutant carrying a mutation near the C terminus (C-terminal sequence: FTD (wild-type)→VH (mutant)), thus truncating the protein near the C terminus. The VH mutant lacks the ability to form filaments but retains the ability to form pores. In accordance with its pore-forming activity, the RegIIIα VH mutant retained membrane toxicity against liposomes and live bacteria. In fact, membrane toxicity was modestly enhanced in the RegIIIα VH mutant, suggesting that trapping of the pore complexes in filaments inhibits their membrane permeabilizing activity. This function contrasts with that of human α-defensin-6 filaments, which directly trap bacteria in 'nanonets'[20]. **a**, 1.0 μM wild-type (wt) and RegIIIα (VH) mutant was added to 10 μM carboxyfluorescein-loaded liposomes and dye release was monitored. The detergent octylglucoside (OG) was added at the end of the experiment to disrupt remaining liposomes. **b**, Initial rate of liposome dye release (10 μM lipid) as a function of wild-type and mutant RegIIIα concentration. **c**, 5.0 μM wild-type or RegIIIα (VH) mutant was assayed for membrane disruptive activity towards whole bacteria using the SYTOX uptake assay described in Fig. 1. Assays were performed in triplicate. Error bars indicate s.d.; ***$P < 0.001$.
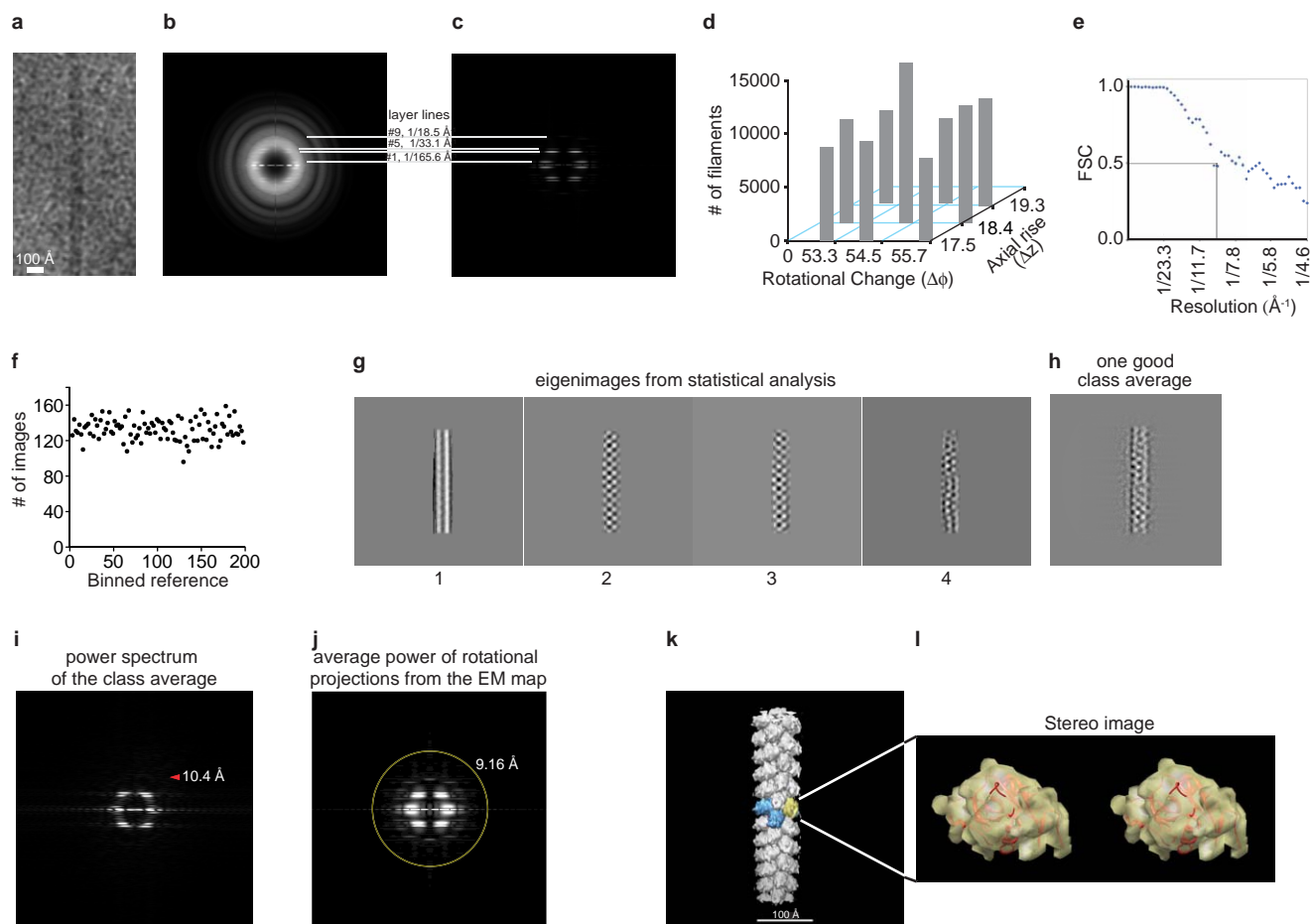
Extended Data Figure 6 | CryoEM reconstruction of the RegIIIα filament structure. **a**, Raw image of a single filament. **b, c**, Comparison of the average power spectrum of cryoEM images of individual short helical segments (**b**) and the average power spectrum (**c**) from the projections of the three-dimensional reconstruction at evenly sampled rotation angles around the helical axis. Layer lines 1, 5 and 9 were labelled, and layer line 4 was clearly visible. **d**, Symmetry variability ($\Delta\varphi$ and Δz) in the cryoEM data set. The reconstruction from the aligned images was imposed with symmetry parameters that vary around the centre pair ($\Delta\varphi = 54.5°$ and $\Delta z = 18.4$ Å), and the experimental data set was classified into nine bins by projection matching. The populations in these classes were exhibited in a three-dimensional histoplot. Even though the central bin is the most populated, the distribution is approximately flat. **e**, Fourier shell correlation (FSC) calculated from the two independent volumes but windowed in different boxes. The strong symmetry in the two volumes led to the FSC ~0.2 at the Nyquist frequency. The first fast drop of FSC curve to 0.5 was elected to give an approximate estimate of resolution. **f**, Number of the filament images aligned with each reference projection from the three-dimensional model in the last round of refinement. The projections from the three-dimensional model evenly sampled the orientation space. As expected, the distribution is fairly flat. **g–j**, Statistical analyses of the RegIIIα filament structure. **g**, First four eigenimages from the multivariate statistical analysis of the centred filaments in the data set that were padded to 320 pixels in size. The second and third images lack mirror symmetry around the central line, suggesting the parity is odd. The fourth image shows the significant local bending of the filaments, a major limiting factor for us in reaching a better resolution in our reconstruction. **h**, A good class average after the multivariate statistical analysis and hierarchical classification. **i**, Square root of calculated power spectrum of the class average in **h**. The tip of the red arrowhead points at 10.4 Å. **j**, The layer lines in the average power spectrum of the rotational projections from the final reconstruction without symmetry imposition extend isotropically to ~9.2 Å (yellow circle), and further along the vertical direction (helical axis). **k, l**, Docking of the RegIIIα crystal structure into the cryoEM map. **k**, The three-dimensional reconstruction calculated from the images in the central bin, **d**, with a hexameric pore highlighted. **l**, Stereo image showing docking of the RegIIIα crystal structure in the cryoEM density map of one subunit out of the reconstruction.

a

Data Collection	
Space group	$P2_12_12_1$
Cell Dimensions	
a, b, c (Å)	30.76, 49.53, 92.15
α, β, γ (°)	90=90=90
Resolution (Å)	50 - 1.47 (1.50 - 1.47)*
R_{sym} (%)	7.0 (55.2)
I/σI	35.5 (2.3)
Completeness (%)	99.5 (94.1)
Redundancy	6.5 (4.3)

Refinement	
Resolution (Å)	26.13 - 1.47 (1.52 - 1.47)
No. reflections	22074
R_{work}/R_{free}	18.5/21.0
No. atoms	
Protein	1901
Ligand/ion	3
Water	181
B-factors	
Protein	19.2
Ligand/ion	23.1
Water	30.0
R.m.s. deviations	
Bond lengths (Å)	1.029
Bond angles (°)	0.006

*Highest resolution shell is shown in parenthesis.

b

Extended Data Figure 7 | Crystal structure of bactericidally active RegIIIα.
a, Table showing data collection and refinement statistics for the active RegIIIα crystal structure. **b**, Crystallographic *B*-factor map of the active RegIIIα structure showing areas of conformational flexibility. Red indicates greater flexibility.
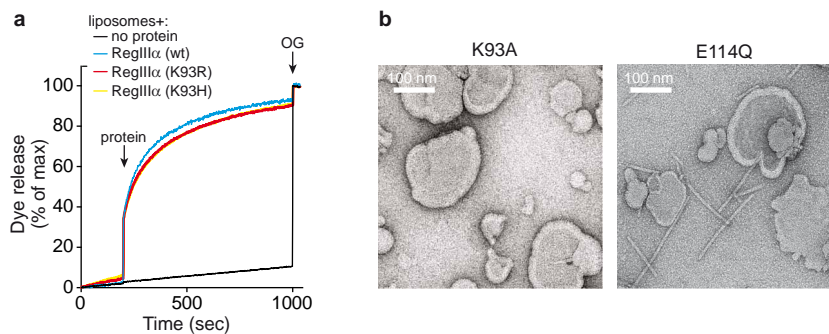
Extended Data Figure 8 | RegIIIα mutagenesis. a, Mutagenesis of Lys 93 (K93) with conservative amino acid substitutions (Arg (R) and His (H)) does not alter membrane toxicity of RegIIIα. 5 μM of wild-type, Lys93Arg mutant, or Lys93His mutant RegIIIα was added to 100 μM carboxyfluorescein-loaded liposomes and dye release was monitored. These mutants retain membrane toxicity, in contrast to Lys93Ala (Fig. 3e), suggesting the importance of positive charges at these sites. **b**, Filamentation of RegIIIα mutants (Lys93Ala (K93A) and Glu114Gln (E114Q)) correlates with membrane toxicity. 20 μM RegIIIα Lys93Ala (left panel) or Glu114Gln (right panel) was incubated for 20 min with unilamellar vesicles and visualized by negative-staining EM. The results demonstrate that the non-toxic Glu114Gln mutant, unlike the toxic Lys93Ala mutant, assembles into filaments.

g

Lipid	K_a (N/Å)	K_c (N·Å)	References
POPC	2.13×10^{-11}	8.5×10^{-10}	22,23
DOPS	nd	4.1×10^{-10}	24,25
GMO	1.425×10^{-11}	2.85×10^{-10}	26,27

nd, not determined

h

Parameter	Value
Electrostatics Grid Dimension	161 x 161 x 161
Electrostatics Coarse Grid Length	240 Å x 240 Å x 240 Å
Electrostatics Fine Grid Length	120 Å x 120 Å x 120 Å
Solvent Dielectric	80
Headgroup Dielectric	80
Membrane Dielectric	2
Protein Dielectric	2
Dipole Potential	300 mV
Bilayer Thickness (d_0)	42 Å
Headgroup Thickness	8.0 Å
Elastic Compression Modulus (K_a)	2.13×10^{-11} N/Å
Elastic Bending Modulus (K_c)	8.5×10^{-10} N·Å
Elastic Stretch Modulus	3.0×10^{-13} N·Å
Elastic Grid Dimension	400 x 400 x 400
Elastic Grid Length	300 Å x 300 Å x 300 Å

Extended Data Figure 9 | Computational modelling of RegIIIα insertion into membranes. **a**, Top-down view of the numeric grid and complex boundary used in the elasticity calculations to represent the upper leaflet. The protein complex occupies the white space in the centre, and the membrane–protein contact curve is the red–white boundary. The membrane is modelled in all non-white regions. The rectangular grid for the elasticity solver is shown here coloured by the membrane bending energy density (red is high bending energy and blue is low bending energy). This calculation corresponds to the membrane bending shown in Fig. 3g. **b–d**, Numeric convergence of the model. **b**, Convergence of the elastostatic energy. In all panels, per cent error was calculated as $100|(E(n) - E(n_{max}))/E(n_{max})|$, where $E(n)$ is energy calculated with n grid points, and n_{max} is maximum number of grid points used. The elastic energy converges smoothly as n increases, and we used $n = 400$ in both the x and y directions for all calculations in the main text, which gives a 5% error. **c**, Convergence of the electrostatic energy. Per cent error of the dipole charge–protein interaction energy (diamonds), protein solvation energy (squares), anionic lipid charge–protein interaction energy (circles) and the total electrostatic energy (triangles) are shown as a function of the grid discretization. A value of $n = 161$ was used for the calculations discussed in the main text resulting in a total electrostatic error of 2.5%. **d**, Convergence of the non-polar energy. A discretization of $n = 100$ points was used for the calculations reported in the main text, and this has a very small error on the order of 0.1%. Values used for calculations in the main text are indicated by an asterisk. **e, f**, Electrostatic potential of the RegIIIα pore complex. **e**, In-plane view. The Poisson–Boltzmann equation was solved using APBS after embedding the complex in a low dielectric region mimicking the lipid bilayer[21]. The low dielectric membrane region is deformed corresponding with the lowest energy shape predicted by our physics-based computational model. Positive (blue) isocontours of the electrostatic potential are drawn at $+5\,\mathrm{kcal\,mol^{-1}\,e^{-1}}$. **f**, Out-of-plane view. All details are identical to those in panel a. Both positive (blue) and negative (red) isocontours of the electrostatic potential are drawn at $\pm5\,\mathrm{kcal\,mol^{-1}\,e^{-1}}$. **g**, Table showing bilayer material properties used in the modelling calculations. **h**, Table showing model parameters. References 24–29 are cited in this figure.

a

b
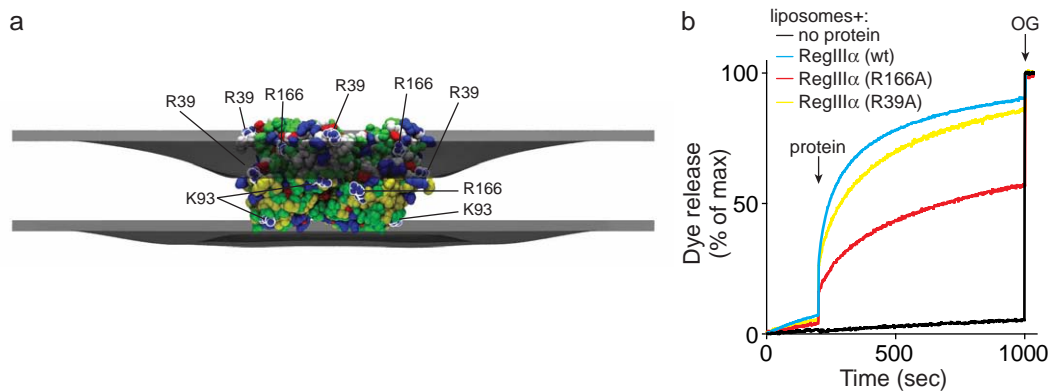
Extended Data Figure 10 | Modelling of RegIIIα–membrane interactions.
a, RegIIIα pore complex model shown from the side. Arg 166 (R166) is located near the water–membrane interface, indicating that it is positioned to interact with the phospholipid head-groups, whereas Arg 39 is predicted to be exposed to aqueous solvent. Membrane boundaries predicted from the computational calculations are indicated. **b**, 5 μM of wild-type, Arg166Ala mutant, or Arg39Ala mutant RegIIIα was added to 100 μM carboxyfluorescein-loaded liposomes and dye release was monitored. The experimental results are consistent with the position of these residues relative to the membrane interface in the model.

20. Chu, H. *et al.* Human α-defensin 6 promotes mucosal innate immunity through self-assembled peptide nanonets. *Science* **337,** 477–481 (2012).
21. Shrake, A. & Rupley, J. A. Environment and exposure to solvent of protein atoms. Lysozyme and insulin. *J. Mol. Biol.* **79,** 351–371 (1973).
22. Henriksen, J. *et al.* Universal behavior of membranes with sterols. *Biophys. J.* **90,** 1639–1649 (2006).
23. Kučerka, N., Tristram-Nagle, S. & Nagle, J. F. Closer look at structure of fully hydrated fluid phase DPPC bilayers. *Biophys. J.* **90,** L83–L85 (2006).
24. Petrache, H. I. *et al.* Structure and fluctuations of charged phosphatidylserine bilayers in the absence of salt. *Biophys. J.* **86,** 1574–1586 (2004).
25. Fuller, N., Benatti, C. R. & Rand, R. P. Curvature and bending constants for phosphatidylserine-containing membranes. *Biophys. J.* **85,** 1667–1674 (2003).
26. Nielsen, C., Goulian, M. & Andersen, O. S. Energetics of inclusion-induced bilayer deformations. *Biophys. J.* **74,** 1966–1983 (1998).
27. White, S. H. Formation of 'solvent-free' black lipid bilayer membranes from glyceryl monooleate dispersed in squalene. *Biophys. J.* **23,** 337–347 (1978).